# SUPPLEMENTARY MATERIAL

## I. Experimental details

### A. Overview of ion-photon source

The cavity-ion-trap system developed for this project (and others) was recently constructed at the Innsbruck IQOQI building. The design is based on that of the system at the nearby University of Innsbruck that was used in [1]. The common design elements are a 20 mm long near-concentric optical cavity with a 3D linear-Paul ion trap hanging (ridgidly) inside it. A key difference is that the present system's cavity parameters are optimised to collect photons near-deterministically, as described in section I B. Full details on the new cavity-integrated ion-trap system will be presented in the upcoming PhD theses of Josef Schupp and Vojtech Krcmarsky.

### B. Cavity parameters

The optical cavity around the ion is near-concentric with a length $l = 19.9057 \pm 0.0003$ mm and radii of curvature $ROC = 9.9841 \pm 0.0007$ mm, determined from simultaneous measurements of the free spectral range (FSR) and higher-order TEM mode spacing (assuming identical mirror geometries) [2]. From this we calculate an expected cavity waist of $\omega_0 = 12.31 \pm 0.07$ $\mu$m and a maximum ion-cavity coupling rate of $g_{\max} = 2\pi \cdot 1.53 \pm 0.01$ MHz. At a wavelength of 854 nm, the finesse of the $\text{TEM}_{00}$ mode is $\mathcal{F} = \frac{2\pi}{\mathcal{L}} = 54000 \pm 1000$, with the total cavity losses $\mathcal{L} = T_1 + T_2 + L_{1+2} = 116 \pm 2$ ppm, determined from measurements of the cavity ringdown time $\tau_{\text{C}} = \frac{\mathcal{F}}{\pi} \cdot \frac{l}{c_0}$, with $c_0$ the speed of light in vacuum. From this one can calculate the cavity linewidth $2\kappa = 2\pi \cdot 140 \pm 3$ kHz, $\kappa$ being the half-width at half maximum.

The transmission $T_{1,2}$ of our cavity mirrors (polishing of the mirror substrates done by Perkins Precision Development, Boulder (Colorado); coating done by Advanced Thin Films) was verified by applying the method described in [3], yielding $T_1 = 2.2 \pm 0.3$ ppm, $T_2 = 97 \pm 4$ ppm, such that the combined mirror losses from scattering and absorption $L_{1+2} = 17 \pm 5$ ppm.

From this one can calculate the probability that a photon inside the cavity exits through mirror $T_2$ (designated output mirror) as $P_{\text{out}}^{\max} = T_2/(T_1 + T_2 + L_{1+2}) = 0.83 \pm 0.03$. $P_{\text{out}}^{\max}$ is therefore the maximum photon collection probability from the ion in our system (with the current mirrors). The system of [1] has $P_{\text{out}}^{\max} = 0.16$.

The cavity length is stabilised via the Pound-Drever-Hall (PDH) method [4] to a laser at 806 nm with a linewidth on the order of 1 kHz [5]. The 806 nm wavelength lies far from any transition in $^{40}\text{Ca}^+$ to minimise AC Stark shifts on the ionic transitions. The cavity is locked to a $\text{TEM}_{01}$ mode and the ions sits in the central intensity minimum to further minimise AC Stark shifts.

The cavity waist is centred on the ion via course tuning of a 3D piezo stick-slip translation-stage system (Attocube). Before experiments, photon generation efficiency is optimised by placing the ion in a cavity antinode. This is done via fine tuning of the cavity position along its axis by applying a small bias voltage to the corresponding piezo stage.

Some key challenges that were overcome to realise our cavity parameters are now briefly described. A complete presentation will be part of the upcoming thesis of Josef Schupp. First, the super polishing of the surfaces of such tightly curved (10 mm ROC) mirror substrates seems not to be a commercially available process as standard and we are therefore grateful to Perkins Precision, Boulder, who did it as a custom job, achieving an RMS roughness of 1 $\pm 0.2$ Å and 1.5 ppm scattering losses on a test piece from the batch. Second, mirror coating via ion beam sputtering was performed by Advanced Thin Films, leading to a mirror pair with total scattering and absorption losses of 9 ppm in our near-concentric configuration. Third, the observed birefringence of cavities built using these mirrors could be minimised by rotating mirror pairs w.r.t. each other, leading to a sub-linewidth $(2 \cdot \kappa)$ splitting of 14 $\pm 2$ kHz in the final cavity (measured by the method of [6]). The fourth step involved a multi-stage procedure to glue the mirrors into position to achieve the near-concentric cavity (the mirrors are glued into metal rings, in turn glued to piezos for cavity-length stabilisation, in turn glued to a rigid metal spacer spanning the cavity length: the only tuneable parameter once glued is the cavity length). The fifth and final key step was for the cavity to survive the ion-trap chamber vacuum baking process, which was achieved by baking at 80 °C, limited by the glass transition temperature of the cavity glue.

### C. Polarisation maintaining single photon conversion setup

A detailed schematic of the photon conversion system is presented in Figure 1. Details about the operation and characterisation of the system (using classical 854 nm laser light) can be found in [7]. Figure 1 provides more details about the pump laser path, the location of the 50 km fibre spool w.r.t. to the filtering network and the final filters employed (a long pass filter, with 1440 nm cutoff, has here been removed after photon conversion since the 50 km fibre spool performs an equivalent task of attenuating weakly phased-matched frequency-doubled pump laser light). We now provide a short summary of the conversion setup.

Difference frequency generation (DFG) is used to convert a 854 nm photon to 1550 nm via a $\chi^{(2)}$ nonlinearity in a 48 mm long PPLN ridge waveguide-integrated chips produced by NTT electronics) $(854\text{ nm})^{-1} - (1902\text{ nm})^{-1} \approx (1550\text{ nm})^{-1}$. Two chips are used in se-

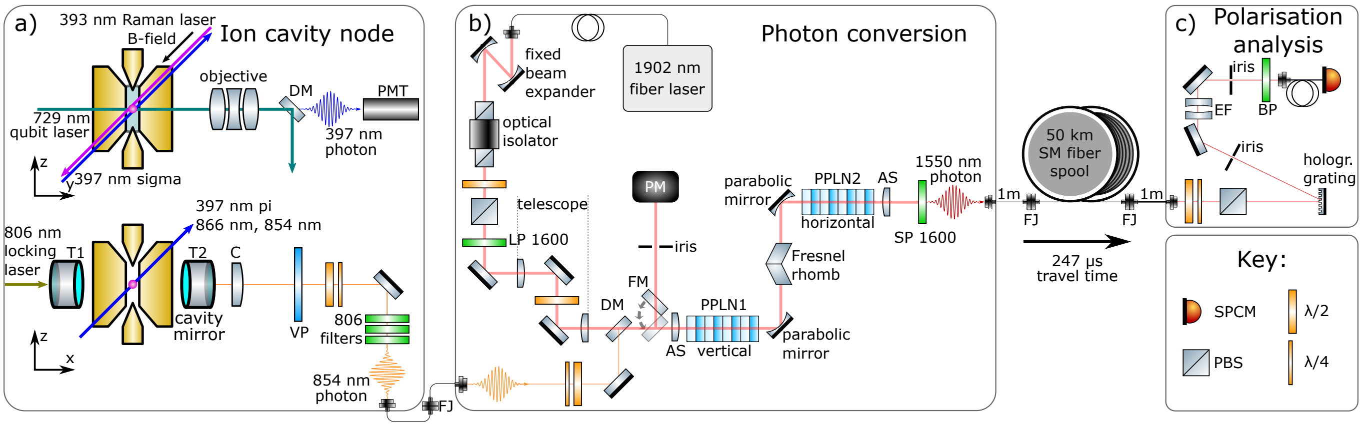


FIG. 1. **Detailed experimental diagram. a) Ion cavity node**. A single atomic ion (red sphere) in the centre of both a 3D radio-frequency (RF) linear Paul trap (gold electrodes) and an optical cavity. The two smaller electrodes are 'end-caps' held at DC voltage. The two larger electrodes are driven with RF, two additional larger electrodes exist but are not shown. Two cross sections are depicted: **Along the cavity axis (top)**, showing: the $\approx 4$ Gauss DC magnetic field (quantisation axis) generated by rings of permanent magnets; the circularly-polarised Raman laser for generating 854 nm cavity photons; the 729 nm laser for ion-qubit manipulation and measurement (see I D); a custom objective (NA = 0.289, $f = 66.8$ mm, lying in an inverted viewport) for collecting spontaneously scattered 397 nm photons for ion-qubit state detection (PMT: Photo multiplier tube). The circularly polarised 397 nm sigma beam is used for optical pumping. **Perpendicular to the cavity axis (bottom)**: Following a Raman pulse, an 854 nm cavity photon exits the cavity via the right mirror with transmission T2 with probability $\geq 0.5 \pm 0.1$ (see II A). The photon then passes the following elements: in-vacuum collimating lens C; vacuum chamber viewport VP; waveplates (for polarisation analysis of 854 nm photon, see IV); 3 filters to remove the 806 nm laser light to which cavity length is continuously and actively stabilised (see I B). The 854 nm photon is then coupled into a single mode fibre (non-polarisation maintaining) leading to the photon conversion setup (total length 10 m with fibre-fibre joiner, FJ). The 397 nm pi beam is used for Doppler cooling and ion-qubit state detection. **b) Photon conversion.** The injected 854 nm photon passes waveplates (used for system setup with classical light) and is overlapped with 1 W of 1902 nm laser light (Tm-doped fibre laser, AdValue Photonics AP-SF1-1901.4-01-LP) on a dichroic mirror (DM) and free-space coupled into one of the ridge waveguides of temperature-stabilised PPLN1 using an asphere (AS, 11 mm, positioned by an XYZ translation stage). The 1902 nm input path includes: beam expander to reduce the beam diameter so as to fit an optical isolator; waveplate and polariser to tune the power; longpass filter (LP 1600 nm) to reduce 1500 nm photons produced directly by the fibre laser; simple telescope to optimise the coupling efficiency to the waveguide. A flip mirror (FM) before PPLN1, and subsequent classical power meter (PM) allows for verifying spatial overlap of the 1902 nm and 854 nm fields (with classical 854 nm light). Gold parabolic mirrors are used to focus/collimate all fields ($f = 15$ mm). A Fresnel rhomb is used to flip polarisation for subsequent conversion of the qubit's other polarisation component in PPLN2. SP 1600 nm: shortpass filter (OD5 at 1902 nm). 50 km fibre spool (Corning SMF-28 ultra, Fiontec). **c) Polarisation analysis.** Hologr. grating: volume holographic Bragg grating (reflection bandwidth 0.2 nm [25 GHz], 95% reflection); EF: air-spaced Fabry-Pérot cavity (250 MHz linewidth, 12.5 GHz free spectral range, peak transmission 95% at 1550 nm, extinction $10^3$); BP: bandpass 1550 nm filter (12 nm bandwidth and 95% transmission). The total conversion efficiency given in the main text (25 $\pm$ 0.02 %) is the probability of getting a 1550 nm photon (from the ion) in the fibre immediately before the single photon counting module (SPCM, InGaAs ID230, IDQuantique), given a fibre-coupled 854 nm input photon in the input fibre to the conversion setup, in the case where the 50 km fibre spool is removed and the waveplates in the polarisation analaysis are set to maximise subsequent PBS transmission.

ries to convert orthogonally-polarisation components of the 854 nm photon sequentially (while the ridge guides support all polarisations, they each convert only one polarisation component). Specifically, in our system, each waveguide converts the vertically-polarised components of the fields. The Fresnel rhomb between the chips (equivalent to a broadband half-waveplate) acts to rotate horizontal to vertical polarisations of all three fields, such that the second chip converts the orthogonal polarisation components to the first chip (see description in [7]).

200 mW of vertically-polarised 1902 nm pump is required in each PPLN for maximum conversion efficiency. To achieve this we send in a total of $\approx$ 1 W of 1902 nm light at the input to PPLN1, with polarisation set to achieved a balanced and maximum conversion efficiency in each PPLN chip.

For extracting the single telecom photon at the output, a filter network consists of a short-pass (OD5 for 1902 nm, cutoff 1600 nm) for reducing the pump power, a volume holographic Bragg grating (bandwidth 0.2 nm) and an etalon (bandwidth 250 MHz) for reducing the 1550 nm noise photons from anti-Stokes Raman scattering, allowing 40 cps photon noise with optimal pump power.

In [7] results from a detailed study of the photon noise introduced by our photon convertor is presented. In summary, the dominant source of photon noise around

1550 nm is Anti-Stokes Raman (ASR) scattering of the pump laser: the process whereby pump laser photons at 1902 nm gain energy (get up-shifted to telecom) by scattering with energetic phonons inside the conversion waveguide. The ASR scattering (added photon noise) in our converter is spectrally white at telecom and can thus be reduced by narrowing the output filtering bandwidth. We achieve a few Hz added photon noise for a filtering bandwidth of 12 GHz, far from the ion-photon linewidth of 0.1 MHz (so narrower filtering would be possible, but is unnecessary). Note that the low noise achieved in our system was enabled by careful choice of initial ion-photon wavelength, allowing for a broad spectral separation between pump laser wavelength and 1550 nm (and therefore minimal ASR noise at telecom). As discussed in section IV, imperfections introduced by the converter into the ion-photon entangled state are consistent (to within statistical uncertainty) with the expected (indepedently-measured) effects of detector dark counts and added photon noise. That is: no other source of error (e.g. imperfect polarisation preservation) could be distinguished within statistical uncertainty. For a detailed analysis of the polarisation preservation of the converter see [7].

### D. *Pulse sequence for 50 km experiment*

Figure 2 shows the laser pulse sequence for the 50 km ion-photon entanglement experiment,the sequence is described in the main text Methods B, a Brief explanation is given in the caption. See also Fig. 3 for the detailed level scheme.

## II. Photon distribution efficiency

In this section information is presented on the efficiency with which photons are distributed in the 50 km experiment and the sources of photon loss.

### A. *Current setup efficiency*

In the 50 km experiment, the total probability that a Raman photon generation pulse leads to a photon click after 50 km is $5.3\times10^{-4}$ (after summing up the outcomes of all polarisation projections).

The total probability of obtaining an on-demand free-space photon out of the ion vacuum chamber is $P_{\mathrm{out}} = 0.5\pm\ 0.1$. This value is inferred from the measured efficiency with which we detect single-mode fibre-coupled (ion-entangled) photons at 854 nm (before the conversion stage), after correcting for the measured 1st fibre-coupling stage efficiency and the known 854 nm photon detector efficiency. The uncertainty in $P_{\mathrm{out}}$ is dominated by the uncertainty in the 1st fibre-coupling stage efficiency, which could be reduced in future.

The overall efficiency of the frequency-conversion setup, including spectral filtering, is $0.25\ \pm\ 0.02$, measured with classical 854 nm light. For a detailed description see [7]. A short overview of the contributing photon losses are summarised in table I. Multiplying all the transmissions together leads to a total expected probability of detecting the photon after 50 km of $(6.5\pm1.5)\times10^{-4}$, which is consistent to within one standard deviation with the measured value of $5.3\times10^{-4}$.

| Location in the photon path | Efficiency |
|---|---|
| On demand photon out of cavity $P_{\mathrm{out}}$ | $0.5\pm0.1$ |
| $1^{\mathrm{st}}$ single-mode fibre coupling | $0.5\pm0.1$ |
| Telecom conversion stage (& filtering) | $0.25\pm0.02$ |
| 50 km fibre transmission | $0.104\pm0.005$ |
| Telecom photon detector efficiency | $0.10\pm0.01$ |
| Expected 50 km detection probability | $(6.5\pm1.6)\times10^{-4}$ |

TABLE I. Photon losses in our 50 km photon distribution experiment. See Figure 1 for the respective locations in the experimental setup.

A total 50 km detection probability of 0.01 should be straightforward to achieve. For example, while in this work an avalanche photo diode detector with 10% efficiency was used, we have recently installed a superconducting nonowire based system from Scontel that provides 0.8 dark cps and 77% efficiency at telecom due to careful filtering of the black body radiation. The company also offers systems with < 10 dark cps and 85-90% efficiency. Similar characteristics with 80-90% efficiency at 5 dark cps were offered by Photonspot. Since taking the data presented in this paper, we have improved the 1st fibre-coupling stage efficiency to 0.8±0.1 and further improvements should be possible. These changes alone are sufficient to achieve a total 50 km efficiency above 0.01.

The efficiency $P_{\mathrm{out}}$ in our setup is limited by losses in our mirror coatings to $P_{\mathrm{out}}^{\mathrm{max}} = 0.83\pm0.03$. Numerical simulations show that it should be possible to get close to this value in our experiment [9] (that is, the probability of the ion emitting into the cavity mode could be $\sim 95\%$) and in recent experiments with our system $P_{\mathrm{out}}\approx0.7$ was achieved by cooling the ion close to the ground state (and thereby enhancing the coupling strength of the cavity-mediated Raman transition, in comparison to the detrimental $P_{3/2}$-state spontaneous scattering rate).

Finally, the achieved photon conversion stage efficiency is predominantly limited by unwanted excitation of higher-order spatial modes in the involved PPLN ridge waveguides [7]. A total device efficiency of 0.5 should be within reach with more careful attention to coupling into the guides and minimising other passive optical losses (e. g. avoiding unnecessary fiber joints). Combing all of the aforementioned improvements would lead to a total 50 km detection probability of nearly 0.03, close to the 50 km fibre transmission of 0.1.

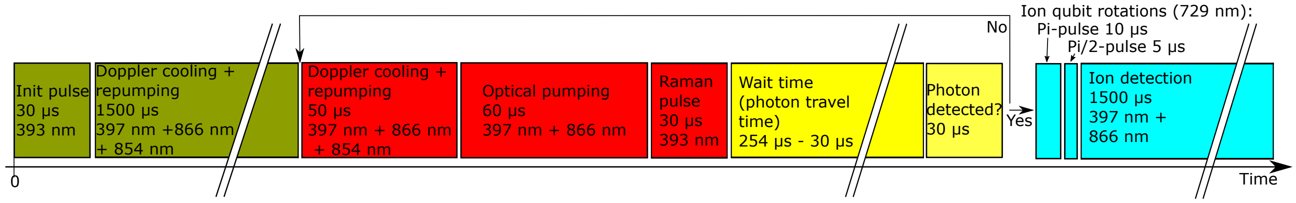


FIG. 2. **Laser pulse sequence for the experiment.** The starting sequence (shown in green) consists of an initialisation laser pulse for intensity stabilisation and Doppler cooling. The loop (shown in red and yellow) consists of additional Doppler cooling, optical pumping, a (photon generation) Raman pulse, a wait time as the photon travels through the 50 km fiber to the detector and a detection window. If the photon detector clicks during within this window, ion qubit manipulation and state detection (shown in blue) are performed, otherwise the loop repeats.

Note that lower loss telecom fibres than the one used here are available (0.16 dB/km, Corning SMF-28 ULL) with a corresponding 50 km transmission of 0.16 and any improvement in fibre technology will further increase that value.

### III. State characterisation

To reconstruct the ion-photon state, a full state tomography of the two-qubit system is performed. On the photon polarisation qubit side, the state is projected to one of 6 states (horizontal, vertical, diagonal, anti-diagonal, right circular and left circular) by waveplates and polariser. This is equivalent to performing projective measurements in three bases described by the Pauli spin-1/2 operators. For example, horizontal and vertical are the eigenstates of the Pauli $\sigma_z$ operator. On the ion qubit side, measurement is performed in the three Pauli bases as described in the main text, Methods B.

For each of the 9 possible joint measurement bases (choice of photon basis and ion basis), the numbers of events corresponding to one of the four possible outcomes of these 2-qubit measurements are considered. We then divide the number of events recorded for each outcome by the total number of events recorded for the given basis (divide each number by the sum of four) and thus obtain estimates of the outcome probabilities. These probabilities are used to reconstruct the 2-qubit state density matrix by linear search with subsequent Maximum Likelihood method [10]. The values of fidelity, concurrence and other measures presented in the main text are calculated using reconstructed density matrices for each of the experiments.

For statistical analysis (determining error bars in quantities derived from the reconstructed density matrix), the Monte-Carlo approach was implemented [11]. Briefly, we numerically generate M = 200 sets of 36 event numbers with Poissonian distribution and mean value equal to the experimental value for each of the 36 possible outcomes. From these simulated event numbers we derive simulated outcome probabilities, the same way as we do for the experimental counts. Then we reconstruct M density matrices for this simulated data and for each one we calculate the quantities of interest (fidelity, concurrence). The error bars given in the main text represent one standard deviation in the widths of the distributions of these quantities over M simulated data sets.

We quantify the state quality in terms of fidelity $F^{\mathrm{m}}$ defined as $F^{\mathrm{m}} = \left[\mathrm{Tr}\sqrt{\sqrt{\rho_{\mathrm{exp}}}\rho_{\mathrm{max.ent.}}\sqrt{\rho_{\mathrm{exp}}}}\right]^2$, where $\rho_{\mathrm{exp}}$ is the density matrix, reconstructed from the experiment data and $\rho_{\mathrm{max.ent.}}$ is the density matrix of the nearest maximally-entangled pure state. This nearest state is found by exposing a perfect Bell state to single qubit unitary rotations and searching for a state providing the best fidelity with the experimentally obtained one.

### IV. Imperfections in the entangled state

Sources of infidelity in the experimentally-reconstructed ion-photon entangled state given in the main text are now analysed. As we will show, the 50 km ion-photon state infidelity can be accounted for (to within statistical uncertainty) by taking into account background detector counts and imperfections in the initial ion-854 nm photon state output from the ion-trap.

Three independent experiments are performed, corresponding to state tomography of the ion-photon state at three different points in the path: First the ion-854 nm photon state immediately at the cavity output (using free space polarisation analysis and two single-mode fibre-coupled 854 nm photon detectors, one at each port of a polarising beam splitter): Second, the ion-1550 nm photon state immediately after conversion (with only a 1 m telecom fibre), referred to as 0 km distance: Third, the ion-1550 nm photon state after 50 km travel (as presented in the main text). The reconstructed state fidelities, with maximally entangled states, are presented in table II (bottom row 'Experiment').

The effect of background photon detector counts is analysed (defined as a detector click that didn't result from a photon from the ion). For this, the background count rate is extracted from the measured counts in the tomography experiments by looking far outside the time window in which the ion-photon arrives, giving 2±0.1 cps for the 1550 nm photon at 50 km and 10±1 cps for the 854

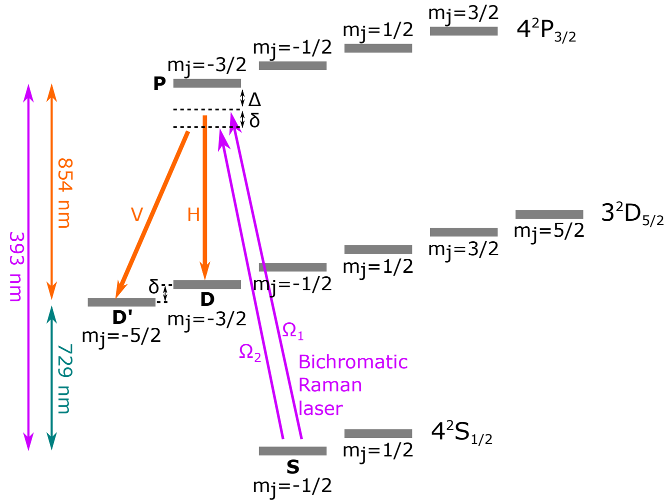


FIG. 3. Relevant energy level scheme of $^{40}Ca^+$. The cavity-mediated Raman transition (CMRT) is shown, for generating an 854 nm photon that is polarisation entangled with the final electronic state of the ion. For details on the CMRT, and the generation of the ion-photon polarisation entangled state see the publication [1] and the PhD thesis [8]. In summary, following optical pumping, the ion (single outer valence electron) begins in the state S. A bichromatic 393 nm Raman pulse is applied with a frequency splitting equal to that of the $D-D'$ states. The bichromatic field and an optical cavity locked to the 854 nm transition generate two Raman processes, leading to the total transformation $|S,0\rangle \rightarrow 1\sqrt{2}(|D,H\rangle + |D',V\rangle$, where 0, $H$ and $V$ are: 0 photons, a single horizontally-polarised and a single vertically-polarised photon in the cavity, respectively. H stands for the linear polarization along the B-field quantization axis ($\pi$-photons). The V polarization stands for the orthogonal linear polarization, produced by the projection of the $\sigma$-polarized photons into the plane perpendicular to the cavity direction (and perpendicular to the B-field quantization axis). The relative amplitude of the two terms in the entangled superposition state are balanced in a separate calibration stage (see [8]), controlled via the relative intensities of the two frequency components in the Raman beam. The phase of the entangled state can be controlled via the relative phase of the two frequency components in the Raman beam. The detuning $\Delta = 409 \pm 10$ MHz. In experiments we set the Rabi frequencies $\Omega_1$ and $\Omega_2$ so as to produce both polarisations with equal probabilities, as described in [1]. The total AC Stark shift exerted by the bichromatic Raman laser on the $S$ state was measured (via 729 nm spectroscopy) to be $AC = 2\pi \cdot (1.14 \pm 0.05)$ MHz, where $AC = \Omega_1^2/4\Delta + \Omega_2^2/4(\Delta+\delta)$.

photon, which are both in agreement with the telecom (1.9±0.15 cps) and 854 nm (10.1±0.9 and 10.8±1 cps) detectors' dark count rates (measured independently). For the 1550 nm photon at 0 km we get $4 \pm 0.1$ cps, where the additional 2 cps background is produced by the photon conversion pump laser anti-Stokes Raman scattering which was reported in [7]. Note that this added noise is attenuated at the same rate as the photons from the ion over the 50 km, and so becomes a small contribution to the background compared to the intrinsic detector dark counts (which do not attenuate over distance).

The infidelity that the background counts would contribute when applied to a perfect maximally-entangled Bell state is simulated numerically. Specifically, the expected background count probability in our photon time-window is added to the expected measurement outcome probabilities for a perfect state, then a new 'noisy' state density matrix is reconstructed via Maximum Likelihood tomography. We call this approach 'Model 1', which simulates the effect of measured background counts only, and find that it explains the majority of the infidelity in the 50 km state (see Table II).

| Fidelity, % | 854nm@0km | 1550@0km | 1550@50km |
|---|---|---|---|
| Model 1 | 99.5 | 96 | 86 |
| Model 2 | - | 93 | 83 |
| Experiment | $96.7 \pm 0.6$ | 92± 2 | 86±3 |

TABLE II. Comparison of modelled and measured ion-photon entangled state fidelities. Model 1: ideal Bell state subjected to background counts during photon qubit measurement. Model 2: Experimentally reconstructed 854 nm state affected by background counts.

In addition to the background counts, Model 2 takes the measured imperfect 854 nm ion-photon state into account. That is, the tomographically reconstructed ion-854 nm-photon state is used as the state to which background counts are added as with Model 1. The results, shown in table II, show that background counts and imperfections in the initial 854 nm state explain the state infidelities to within statistical uncertainty.

Since the imperfections introduced into the ion-photon state by the converter are consistent with those expected from added photon noise and detector dark counts, any other sources of imperfections (e.g. polarisation contrast loss - see [7] for a detailed analysis) cannot be resolved above the $\sim 1\%$ infidelity level.

Regarding infidelities in the initial ion-854 nm photon state: the fidelity in this case is limited by the state purity ($Tr(\rho^2) = 0.94 \pm 0.01$, where $\rho$ is the 854 nm reconstructed state) meaning that only the imperfections leading to decoherence (or effective decoherence) need be considered. Possible error sources include errors in the 729 nm laser pulses used to determine the ion measurement basis, decoherence of the ion-qubit due to e.g. fluctuating magnetic fields and relative intensity fluctuations of the two frequency components in the Raman drive leading to a mixture of different states over the duration of the experiment. Identifying the size and relative contribution of these errors is beyond the scope of this work. The achieved fidelity at 854 nm is similar to that achieved in [1].

[1] Stute, A. et al.. Tunable ion-photon entanglement in an optical cavity. Nature **485**, 482 (2012).

[2] Siegman, A. Lasers. University Science Books (1986).

[3] Hood, C. J., Kimble, H. J. & Ye, J. Characterization of high-finesse mirrors: Loss, phase shifts, and mode structure in an optical cavity. Phys. Rev. A **64**, 033804 (2001).

[4] Black, E. D. An introduction to pound–drever–hall laser frequency stabilization. American Journal of Physics **69**, 1, 79 (2001).

[5] Hainzer, H. Laser Locking For Trapped-Ion Quantum Networks. Diplomarbeit, University of Innsbruck (2018).

[6] Fleisher, A. J., Long, D. A., Liu, Q. & Hodges, J. T. Precision interferometric measurements of mirror birefringence in high-finesse optical resonators. Phys. Rev. A **93**, 013833 (2016).

[7] Krutyanskiy, V., Meraner, M., Schupp, J. & Lanyon, B. P. Polarisation-preserving photon frequency conversion from a trapped-ion-compatible wavelength to the telecom c-band. Applied Physics B **123**, 9, 228 (2017).

[8] Stute, A. A light-matter quantum interface: ion-photon entanglement and state mapping. Dissertation, University of Innsbruck (2013).

[9] Maurer, C., Becher, C., Russo, C., Eschner, J. & Blatt, R. A single-photon source based on a single ca + ion. New Journal of Physics **6**, 1, 94 (2004).

[10] Hradil, Z., Summhammer, J. & Rauch, H. Quantum tomography as normalization of incompatible observations. Physics Letters A **261**, 1, 20 (1999).

[11] Efron, B. & Tibshirani, R. Bootstrap methods for standard errors, confidence intervals, and other measures of statistical accuracy. Statist. Sci. **1**, 1, 54 (1986).